Physical mechanisms controlling self-aggregation of convection in idealized numerical modeling simulations

Allison A. Wing[1] and Kerry A. Emanuel[1]

[1] We elucidate the physics of self-aggregation by applying a new diagnostic technique to the output of a cloud resolving model. Specifically, the System for Atmospheric Modeling is used to perform 3- D cloud system resolving simulations of radiative-convective equilibrium in a nonrotating framework, with interactive radiation and surface fluxes and fixed sea surface temperature (SST). We note that self-aggregation begins as a dry patch that expands, eventually forcing all the convection into a single clump. Thus, when examining the initiation of self-aggregation, we focus on processes that can amplify this initial dry patch. We introduce a novel method to quantify the magnitudes of the various feedbacks that control self-aggregation within the framework of the budget for the spatial variance of column-integrated frozen moist static energy. The absorption of shortwave radiation by atmospheric water vapor is found to be a key positive feedback in the evolution of aggregation. In addition, we find a positive wind speed-surface flux feedback whose role is to counteract a negative feedback due to the effect of air-sea enthalpy disequilibrium on surface fluxes. The longwave radiation feedback can be either positive or negative in the early and intermediate stages of aggregation; however, it is the dominant positive feedback that maintains the aggregated state once it develops. Importantly, the mechanisms that maintain the aggregate state are distinct from those that instigate the evolution of self-aggregation.

Citation: Wing, A. A., and K. A. Emanuel (2013), Physical mechanisms controlling self-aggregation of convection in idealized numerical modeling simulations, *J. Adv. Model. Earth. Syst.*, 5, doi:10.1002/2013MS000269.

1. Introduction

[2] Moist convection in the tropical atmosphere is often organized into clusters containing many individual convective cells. This organized convection spans a range of scales, from squall lines (~10 km) [e.g., *Houze*, 1977], to mesoscale convective complexes (~100 km) [e.g., *Maddox*, 1980], to tropical cyclones (~1000 km) [e.g., *Simpson et al.*, 1997; *Challa and Pfeffer*, 1990; *Lee*, 1989] to the Madden-Julian Oscillation (~10,000 km) [e.g., *Madden and Julian*, 1971]. Clusters of organized convection are ubiquitous in the tropics [*Mapes et al.*, 2009; *Futyan and Del Genio*, 2007; *Houze*, 2004; *Nesbitt et al.*, 2000; *Machado and Rossow*, 1993; *Mapes and Houze*, 1993] and have important impacts on weather and climate. For instance, convective cloud clusters are responsible for much of the rainfall and cloudiness over the tropics, with approximately 50% of tropical rainfall due to mesoscale convective systems [*Nesbitt et al.*,

2000]. Tropical cloud clusters modulate the radiative heating of the surface and atmosphere and influence the large-scale circulation and moisture distribution of the atmosphere. In idealized modeling studies [e.g., *Bretherton et al.*, 2005], the development of large-scale convective organization alters the mean vertical profiles of temperature, moisture, and radiative fluxes, highlighting the potentially important effect of organized convection on variables important to climate. *Tobin et al.* [2012] found a systematic dependence of water vapor, turbulent surface fluxes, and radiation on the degree of convective aggregation in observations. They found that aggregated convection is associated with lower free tropospheric humidity in the nonconvecting environment, enhanced turbulent surface fluxes within and outside convective areas, and reduced low to mid-level cloudiness in the environment. Understanding how and why tropical convection organizes is important for understanding both tropical and global climate variability, and climate sensitivity.

[3] Tropical convection is often viewed as a quasi-equilibrium process in which convective clouds consume convective available potential energy at the same rate it is supplied by large-scale processes [*Arakawa and Schubert*, 1974]. The simplest form of such an equilibrium is radiative-convective equilibrium (RCE), in

---

[1]Program in Atmospheres, Oceans, and Climate, Department of Earth, Atmospheric, and Planetary Sciences, Massachusetts Institute of Technology, Cambridge, Massachusetts, USA
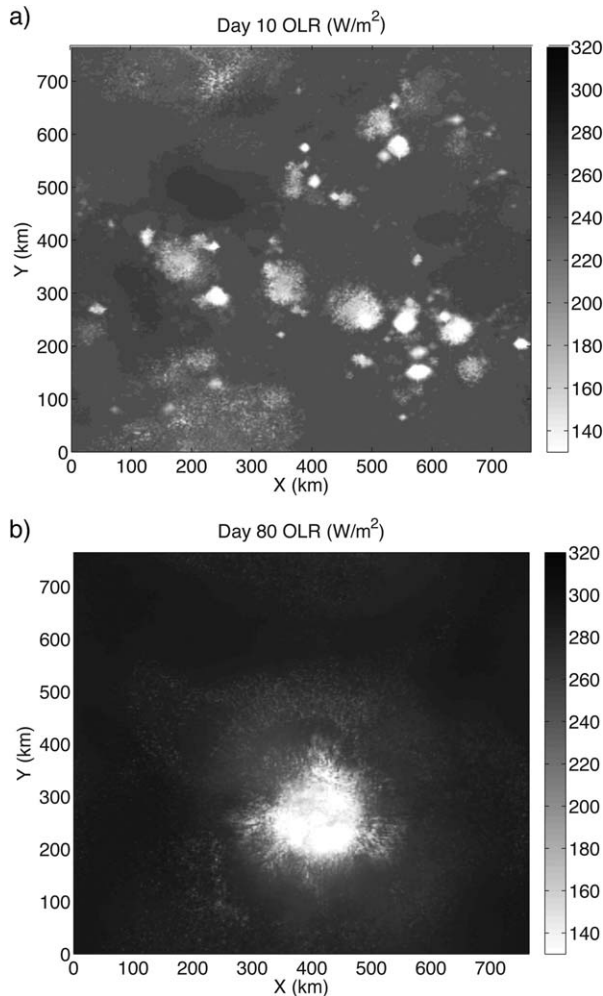
a)

Day 10 OLR (W/m²)

b)

Day 80 OLR (W/m²)

Figure 1. Snapshot of outgoing longwave radiation (OLR) at (a) day 10 and (b) day 80 of a radiative-convective equilibrium simulation at 305 K.

which radiative cooling is balanced by convective heating. On large enough space and time scales, the tropics can be thought of as in RCE, although RCE is not observed locally due to the presence of large-scale atmospheric circulations. Nevertheless, RCE is a good starting point for understanding tropical dynamics. Simulations of convection in RCE using three-dimensional cloud system resolving models often produce distributions of convection that are nearly random in space and in time [*Islam et al.*, 1993]. However, when certain conditions are met, the convection becomes organized into a single, intensely convecting moist cluster surrounded by a broad region of dry subsiding air [*Bretherton et al.*, 2005; *Nolan et al.*, 2007]. Figure 1 shows an example of a three-dimensional RCE simulation that transitions from disorganized convection in the beginning of the simulation (Figure 1a) to a single cluster (Figure 1b) 70 simulated days later. The details of that simulation will be given in section 3.

[4] Convection is often thought of as being organized by external influences such as large-scale sea surface temperature (SST) gradients or wind shears [e.g., *Robe*

and Emanuel, 2001]. However, in the case shown in Figure 1, there are no such external influences. Convection is instead self-organizing through interactions between the environment and the convection and radiation, which is referred to as "self-aggregation." We address three key questions related to self-aggregation:

[5] 1. How does self-aggregation evolve?

[6] 2. What physical feedback mechanisms are important and what are their magnitudes?

[7] 3. How and why does self-aggregation depend on sea surface temperature?

[8] Insights from previous work on self-aggregation are reviewed in section 2 while the model and simulations are described in section 3. Section 4 describes the evolution to a self-aggregated state. In section 5, the analysis framework, which is a budget for the spatial variance of vertically integrated frozen moist static energy, is described. The results of this analysis and quantification of the feedbacks are presented in section 6, and the most important physical mechanisms are discussed in section 7. In section 8, we summarize our key findings and suggest directions for future work. A more detailed exploration of the physical mechanisms and how they determine the temperature dependence of self-aggregation will be provided in a companion paper [*Emanuel et al.*, 2013].

2. Previous Work on Self-Aggregation

[9] Numerous studies over the last two decades have investigated self-organization of convection. In a two-dimensional simulation, *Held et al.* [1993] found a localization of convection in which convective moistening of the atmosphere made the same location favorable for future convection. *Tompkins* [2001] also found that water vapor played an important role in the organization of convection in simulations with a three-dimensional channel domain. Specifically, a cluster of convection moistened its local environment while drying more distant regions, due to the different time scales associated with the moistening and drying of the atmosphere by convective activity. *Bretherton et al.* [2005] found that, in a 100 day radiative-convective equilibrium simulation with a three-dimensional cloud resolving model, convection self-aggregated into a single cluster. They interpreted this phenomenon as driven by convection-water vapor-radiation feedbacks which dry the drier air columns and moisten the moister air columns. The radiative part of the feedback is such that there is enhanced longwave cooling of the driest columns and decreased longwave cooling of the moistest columns.

[10] While most of the studies of self-aggregation have been performed with no rotation, if sufficient rotation is added, the convective clusters in the aggregated state can take the form of tropical cyclones [*Khairoutdinov and Emanuel*, 2012; *Nolan et al.*, 2007; *Bretherton et al.*, 2005]. *Bretherton et al.* [2005] found that simulations with a larger Coriolis parameter aggregated more quickly into an intense tropical cyclone. *Nolan et al.* [2007] found that simulations initiated with random

convection sometimes underwent spontaneous tropical cyclogenesis, caused by radiative-convective feedbacks that generate aggregation; the circulation associated with the self-aggregated state then intensifies and contracts into a tropical cyclone. *Khairoutdinov and Emanuel* [2012] studied the characteristics of RCE on an f-plane by artificially increasing the Coriolis parameter; this allowed them to simulate multiple tropical cyclones in the same domain.

[11] *Held et al.* [1993] and *Nolan et al.* [2007] noted that the localization of convection and spontaneous typical cyclogenesis, respectively, proceeded much more slowly when the SST was lowered. Similarly, it has been found that self-aggregation only occurs above a temperature threshold [*Khairoutdinov and Emanuel*, 2010; *Wing and Emanuel*, 2012]. This may have important consequences. For example, *Khairoutdinov and Emanuel* [2010] hypothesized that the temperature dependence of aggregation could lead to a self-organized critical state, in which the system is attracted to the transition between aggregated and disaggregated states. No explanation has been offered for the SST threshold of self-aggregation found in simulations.

[12] Self-aggregation is sensitive to the domain size and horizontal resolution of the simulations, with aggregation being favored by large domains and relatively coarse resolution [*Muller and Held*, 2012; *Jeevanjee and Romps*, 2013]. Regarding explanations for the domain size dependence of self-aggregation, there are conflicting results in the literature. *Muller and Held* [2012] explain this sensitivity by the dependence of low clouds on domain size, while *Jeevanjee and Romps* [2013] find that cold pools are responsible for the domain size threshold (in the absence of cold pools, self-aggregation occurs at all scales and only weakens as the domain size decreases). *Jeevanjee and Romps* [2013] found that in small domains, a shallow circulation that weakens aggregation dominates. In contrast, *Muller and Held* [2012] argue that a shallow circulation driven by longwave cooling at the top of low clouds provides up-gradient energy transport that is important for aggregation. The role of circulation in providing up-gradient energy transport for aggregation was also highlighted by *Bretherton et al.* [2005].

[13] Previous studies have investigated various feedback mechanisms for self-aggregation primarily by performing mechanism denial experiments in which they attempt to remove the various feedbacks by preventing certain interactions. *Tompkins and Craig* [1998] found that using a wind-independent surface flux calculation destroyed the aggregation (which was characterized by an alignment of convection into a band structure) in their simulations. *Bretherton et al.* [2005] found that horizontally homogenizing the surface fluxes prevented self-aggregation, while *Muller and Held* [2012] found that it did not in all cases. Sensitivity studies performed to determine the conditions under which aggregation does or does not occur, have also indicated that if radiative heating rates are horizontally homogenized, self-aggregation does not occur [*Tompkins and Craig*, 1998; *Bretherton et al.*, 2005]. The importance of interactive radiation was also highlighted by *Stephens et al.* [2008], who found that the banded nature of convective organization in their simulations was established by gradients in radiative heating that are determined by differences in clouds between wet and dry regions, which are in turn controlled by the convection. *Muller and Held* [2012] also found that radiation-cloud interactions were key by performing sensitivity experiments in which they successively turned off various mechanisms. They found that self-aggregation still occurred with homogenized surface fluxes and homogenized shortwave radiative heating, but did not occur with homogenized longwave radiative cooling. Specifically, they argued that the mechanism causing self-aggregation is the longwave radiative cooling from the top of low (liquid water) clouds in the dry regions.

[14] While strides have been made identifying the physical mechanisms causing self-aggregation of convection, there has not been a systematic quantification of the various feedbacks essential to it. This study works toward closing this gap in our understanding of the physics of self-aggregation. To that end, a new analysis technique is applied to radiative-convective equilibrium simulations performed with a cloud resolving model; the details of these simulations are described in the next section.

3. Model Simulations

[15] The model used is the System for Atmospheric Modeling, version 6.8.2, henceforth referred to as SAM [*Khairoutdinov and Randall*, 2003]. SAM was used by *Bretherton et al.* [2005], *Khairoutdinov and Emanuel* [2010], *Muller and Held* [2012], and *Wing and Emanuel* [2012] for investigating self-aggregation. SAM is a three-dimensional cloud resolving model that employs the anelastic equations of motion. The prognostic thermodynamics variables are total nonprecipitating water, total precipitating water, and the liquid water/ice static energy, h_L

$$h_L = c_p T + gz - L_v(q_c + q_r) - L_s(q_i + q_s + q_g), \qquad (1)$$

where q_c is the cloud water mixing ratio, q_r is the rain mixing ratio, q_i is the cloud ice mixing ratio, q_s is the snow mixing ratio, q_g is the graupel mixing ratio, L_v is the latent heat of evaporation, and L_s is the latent heat of sublimation. The total nonprecipitating water mixing ratio is the sum of the mixing ratios of water vapor, cloud water, and cloud ice, while the total precipitating water mixing ratio is the sum of the mixing ratios of rain, snow, and graupel. The diagnosed cloud condensate and total precipitating water are partitioned into hydrometeor mixing ratios at every time step as a function of temperature. The subgrid-scale fluxes are computed using a Smagorinsky-type parameterization, as in *Bretherton et al.* [2005] and *Muller and Held* [2012]. As in previous studies of self-aggregation with SAM, we use the 1-moment microphysics package. Further details about the model can be found in *Khairoutdinov and Randall* [2003].

[16] Longwave and shortwave radiative fluxes are computed using the RRTM radiation scheme [*Mlawer et al.*, 1997; *Clough et al.*, 2005; *Iacono et al.*, 2008] in which the radiative transfer is computed at each individual grid column using the instantaneous model temperature, water vapor, and cloud fields. The solar insolation is constant and equal to a value of 413.98 W/m^2 (following *Bretherton et al.* [2005]) with a zenith angle of 50.5°; there is no diurnal cycle. The surface sensible and latent heat fluxes are computed interactively, using an iterative procedure to compute the exchange coefficients. A minimum wind speed of 1 m/s is used to calculate the surface fluxes. The simulations discussed here are performed with a domain size of 768 × 768 km^2 with 64 vertical levels and rigid lid at 28 km, unless otherwise indicated. A doubly periodic lateral boundary condition is employed. The model grid is a fully staggered Arakawa C-type grid with a uniform horizontal resolution of 3 km and a stretched vertical grid. The lowest model level is at 37 m and the grid spacing is 75 m near the surface, increasing to 500 m above 3.5 km. Newtonian damping is applied to all prognostic variables in a sponge layer covering the upper third of the model domain to reduce gravity wave reflection and buildup. A standard simulation is run for 100 days, with a variable time step of 12 s or less (to satisfy the CFL condition). The model is initialized with a sounding from the domain average of a simulation of radiative-convective equilibrium on a 96 × 96 km^2 domain at the same sea surface temperature. There is no mean wind, no rotation, and no external forcing imposed. Motion is initialized by adding white noise to the initial h_L field at the five lowest grid levels, with an amplitude that is 0.1 K at the lowest model level and decreases linearly to 0.02 K at the fifth model level. The simulations are performed at fixed sea surface temperature (SST), with values between 297 K and 312 K; but most of the results shown in this paper are for the 305 K case.

4. Evolution of Self-Aggregation

[17] We first compare the evolution of domain averaged outgoing longwave radiation (OLR) in each of the simulations performed at different values of SST (Figure 2). The simulations are identical except for the SST (and its corresponding initial sounding). An obvious feature in some of the simulations is a dramatic increase in the OLR, which marks the transition to self-aggregation. OLR increases when convection is aggregated because the domain mean free troposphere is significantly drier when convection is aggregated. Simulations at SST values of 301, 303, 305, and 307 K self-aggregate between 50 and 70 days; simulations at colder and higher values of SST do not aggregate during the period of integration (Figure 2 and Table 1). Table 1 provides additional information about the simulations shown in Figure 2. The table indicates, for each SST, a representative initial and final value for two domain average indicators of self- aggregation: OLR and column relative humidity (CRH). The four simulations that self-aggregated all feature an increase of more than 30 W/m^2 in the OLR between the initial
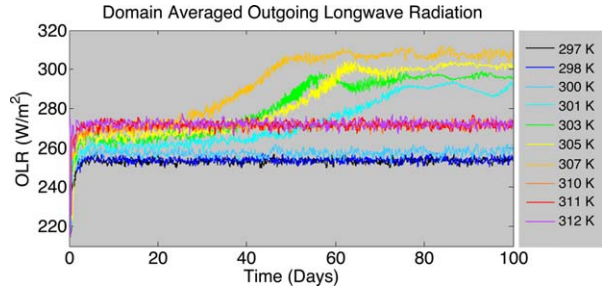

Figure 2. Evolution of the domain averaged outgoing longwave radiation (OLR). Each curve is a simulation performed at a different fixed SST. The data are hourly averages.

and final periods. There is a corresponding large decrease in the CRH.

[18] Based on previous work [*Khairoutdinov and Emanuel*, 2010], we expected that self-aggregation would not occur at the coldest SST's (297–300 K), but it is surprising that self-aggregation does not occur at the highest SST's (310–312 K). Experiments extending the 310 and 312 K SST runs by 40 days still fail to aggregate. We speculated that the high SST simulations required a larger domain size, perhaps because of the large values of dry static stability that occur at high temperature (with a larger static stability, the compensating subsidence is weaker and thus requires a larger area). Indeed, when we reran the 310 K simulation with a domain size of 1536 × 1536 km^2 in the horizontal (four times the area of our original domain), self-aggregation did occur.

[19] Note that the time to aggregation, as approximated by when the OLR stops increasing, does not vary monotonically with SST (Figure 2). This indicates a possibly large stochastic component of self-aggregation. Sensitivity tests in which, for a given SST, we vary the random noise used to initialize the simulations seem to confirm the stochastic nature of self-aggregation, with the time to aggregation varying by about 20 days. The location of the cluster and its spatial orientation (i.e., whether it is an elongated band or a circular cluster)

Table 1. Summary of Domain Average Statistics at Different Fixed SSTs[a]

SST	Self-Aggregates?	OLR$_i$ (W/m^2)	OLR$_f$ (W/m^2)	CRH$_i$	CRH$_f$
297 K	No	253.37	253.54	0.6978	0.6961
298 K	No	253.93	253.86	0.7047	0.7018
300 K	No	257.38	258.36	0.7111	0.6964
301 K	Yes (circular)	259.90	286.57	0.6981	0.4102
303 K	Yes (band)	264.18	296.22	0.7064	0.3345
305 K	Yes (circular)	266.46	302.30	0.7165	0.3195
307 K	Yes (band-circular)	270.75	307.69	0.7073	0.3124
310 K	No	269.92	271.92	0.7582	0.7435
311 K	No	272.10	271.64	0.7521	0.7503
312 K	No	272.18	272.09	0.7528	0.7507

[a]OLR is outgoing longwave radiation, CRH is column relative humidity. The "*i*" subscript indicates an average from day 10 to 20, while the "*f*" subscript indicates an average from day 85 to 100. All quantities are horizontal means.
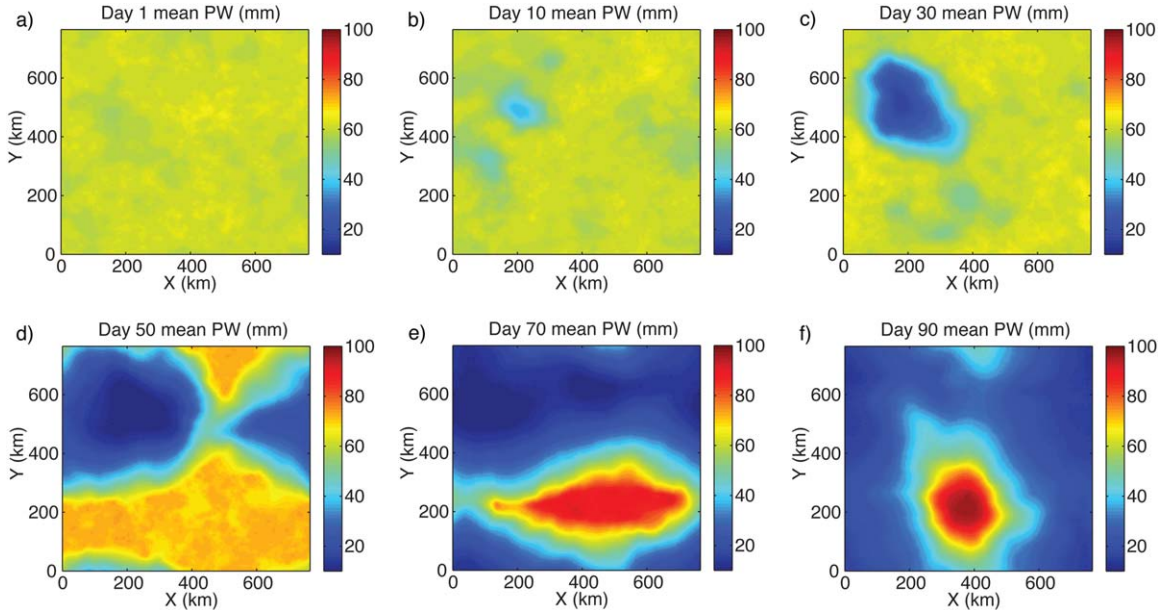
Figure 3. Daily average precipitable water (PW, in mm) for days (a) 1, (b) 10, (c) 30, (d) 50, (e) 70, and (f) 90. The data are from a simulation at 305 K.

also vary with the initial random noise. In some of the simulations, the convection aggregates into an elongated band and stays in this state for 10 s of days before collapsing further into a circular cluster. The type of cluster obtained in the simulations that self-aggregate is indicated in Table 1.

[20] In simulations where self-aggregation occurs, the domain averaged OLR gradually increases over the first 50–70 days of the simulation (Figure 2). To further explore what happens as self-aggregation evolves, we examine the simulation at 305 K as a case study. This temperature is firmly above the threshold for aggregation in our set of simulations but is not so warm that aggregation requires a larger domain. Plan views of daily mean precipitable water (PW) throughout the simulation at 305 K are shown in Figure 3.

[21] The day 1 average precipitable water (PW) field in the 305 K simulation is fairly homogeneous (Figure 3a). By day 10 (Figure 3b), a small area near $X = 200$ km and $Y = 500$ km has become drier than the rest of the domain. Over the next 20 days, the small dry patch amplifies and expands and by day 30 (Figure 3c) it covers nearly a quarter of the domain. This process continues, and at day 50 (Figure 3d) the areas of the domain not in the dry patch have become moister than they were initially. At day 70 (Figure 3e), the expanding dry region has confined all the moist air (which is now much moister than anywhere earlier in the simulation) to one band. This band evolves into a single circular cluster in which high PW values are concentrated, as seen at day 90 (Figure 3f). Outside the moist cluster, the rest of the domain has very low values of PW. These results show that self-aggregation begins as a dry patch that expands. Convection is suppressed in the dry patch and becomes increasingly localized into a single cluster.

Our goal is to understand the feedback mechanisms that allow the dry patch to amplify and expand.

5. Analysis Framework

5.1. Budget for Spatial Variance of FMSE

[22] We frame our analysis in terms of the budget of the spatial variance of vertically integrated frozen moist static energy. The frozen moist static energy (FMSE) is conserved during moist adiabatic processes in the model, including the freezing and melting of precipitation, and is given by

$$h = c_p T + gz + L_v q_v - L_f q_{ice}, \qquad (2)$$

where L_f is the latent heat of fusion, q_v is the water vapor mixing ratio, and q_{ice} represents all ice phase condensates. The FMSE is a desirable diagnostic of self-aggregation because its variance increases as aggregation progresses, and because its mass-weighted vertical integral can only be changed by radiation, surface fluxes, and advection. Convection redistributes FMSE but cannot change its mass-weighted vertical integral. We begin with the budget equation for vertically integrated frozen moist static energy, $\hat{h}$:

$$\frac{\partial \hat{h}}{\partial t} = \mathrm{SEF} + \mathrm{NetSW} + \mathrm{NetLW} - \nabla_h \cdot \vec{\hat{u}} h, \qquad (3)$$

where SEF is the surface enthalpy flux and NetSW and NetLW are the column shortwave and longwave radiative flux convergences, respectively. The "$\hat{x}$" notation indicates a density-weighted vertical integral, $\int_0^{z_{top}} [] \rho \, dz$. The surface enthalpy flux, SEF, is defined as the sum of

the latent and sensible heat fluxes, (LHF and SHF, respectively), which are given by the standard bulk formulae:

$$LHF = \rho c_E L_v U \left(q_{T_s}^* - q_v \right) \qquad (4)$$

$$SHF = \rho c_H c_p U (T_s - T_a) \qquad (5)$$

$$SEF = LHF + SHF. \qquad (6)$$

[23] In equations (4) and (5), ρ is the air density at the lowest model level, c_E is the latent heat exchange coefficient, U is the surface wind speed, $q_{T_s}^*$ is the saturation water vapor mixing ratio at the surface temperature, q_v is the water vapor mixing ratio at the lowest model level, c_H is the sensible heat exchange coefficient, T_s is the surface temperature, and T_a is the air temperature at the lowest model level. Hereafter, we will refer to $q_{T_s}^* - q_v$ as Δq and $T_s - T_a$ as ΔT. The column longwave radiative flux convergence is defined as

$$NetLW = LW_{sfc} - LW_{top}, \qquad (7)$$

where LW_{sfc} and LW_{top} are the net longwave fluxes at the surface and top of atmosphere, respectively, where a positive flux is defined to be upward. In the results shown here, the column longwave flux convergence is negative everywhere, indicating that more longwave radiation is exiting the column at the top than entering it at the bottom. The column shortwave radiative flux convergence is defined as

$$NetSW = SW_{top} - SW_{sfc}, \qquad (8)$$

where SW_{top} and SW_{sfc} are the net shortwave fluxes at the top of the atmosphere and surface, respectively, where a positive flux is defined to be downward. The column shortwave flux convergence is positive everywhere, indicating that more shortwave radiation is entering the column at the top than is exiting it from the bottom.

[24] For an arbitrary variable A, we denote the horizontal mean as $\{A\}$ and the anomaly from the horizontal mean as A'. We subtract the horizontal mean of equation (3) from the full form of the equation to obtain an equation for the time rate of change of the anomaly of vertically integrated FMSE, $\hat{h}'$. Finally, multiplying that result by $\hat{h}'$ results in a budget equation for the spatial variance of vertically integrated frozen moist static energy:

$$\frac{1}{2} \frac{\partial \hat{h}'^2}{\partial t} = \hat{h}' SEF' + \hat{h}' NetSW' + \hat{h}' NetLW' - \hat{h}' \nabla_h \cdot \vec{u} h, \qquad (9)$$

in which $\hat{h}'$ indicates the anomaly of the density-weighted vertical integral of FMSE and $\nabla_h \cdot \vec{u} h$ is the horizontal divergence of the density-weighted vertical integral of the flux of FMSE. $\hat{h}' SEF'$, $\hat{h}' NetSW'$, and $\hat{h}' NetLW'$ represent the correlations of $\hat{h}'$ with anomalies in the three diabatic sources and sinks of FMSE: surface enthalpy fluxes, column shortwave convergence, and column longwave convergence, respectively.

5.2. Partitioning of Surface Enthalpy Flux Anomalies

[25] Surface enthalpy fluxes are affected primarily by variations in surface wind speed and by the thermodynamic disequilibrium between the ocean and the overlying atmosphere. We can formally decompose SEF′ into a part due solely to variations in the surface wind speed, a part due solely to variations in the air-sea enthalpy disequilibrium, and an eddy term representing variations due to the product of the two. In the model's surface flux calculation, the exchange coefficients, c_E and c_H, are calculated iteratively and vary in both space and time. An offline calculation using the surface flux code over the range of surface air temperatures, water vapor mixing ratios, and wind speeds observed in the simulations indicated that the exchange coefficients vary strongly with the surface wind speed but only weakly with the air-sea disequilibrium over the range explored. Therefore, the exchange coefficients are combined with the surface wind speed when calculating horizontal means and anomalies from those means. Each of the four variables in equations (4–6), ($c_E U$, $c_H U$, Δq, ΔT), are separated into a mean and an anomaly. Substituting these definitions into equations (4–6) and solving for SEF′, we find that the surface enthalpy flux anomaly can be written as

$$SEF' = \overbrace{\rho L_v (c_E U)' \{\Delta q\} + \rho c_p (c_H U)' \{\Delta T\}}^{(i)}$$

$$+ \overbrace{\rho L_v \{c_E U\} \Delta q' + \rho c_p \{c_H U\} \Delta T'}^{(ii)} \qquad (10)$$

$$+ \overbrace{\rho L_v (c_E U)' \Delta q' + \rho c_p (c_H U)' \Delta T' - \rho L_v \{(c_E U)' \Delta q'\} - \rho c_p \{(c_H U)' \Delta T'\}}^{(iii)}.$$

[26] Term (i) in equation (10) represents the part of the SEF anomaly due solely to variations in the surface wind speed. Term (ii) represents the part of the SEF anomaly due solely to variations in the air-sea enthalpy disequilibrium. Term (iii) represents the part of the SEF anomaly due to the product of variations in the surface wind speed and variations in the air-sea enthalpy disequilibrium, which we refer to as the "eddy term."

5.3. Application to Self-Aggregation

[27] Because self-aggregation is associated with an increase in the variance of vertically integrated FMSE, processes that increase $\hat{h}'^2$ favor self-aggregation. It is then clear from equation (9) that if the correlation between the anomaly of a diabatic term and $\hat{h}'$ is positive, there is either an anomalous source of FMSE in a region of already high FMSE, or an anomalous sink of FMSE in a region of low FMSE. Both of these processes represent a positive feedback on self-aggregation. The four diabatic terms in equation (9), including the decomposition of SEF$'$ according to equation (10), are calculated explicitly in the model at each time step and output as hourly averages, as is $\hat{h}'^2$. We calculate the horizontal convergence term, the last term in equation (9), as a residual from the rest of the budget (as was done for FMSE budget calculations in *Bretherton et al.* [2005] and *Muller and Held* [2012]). We then average each term over a day and over 48×48 km^2 blocks to focus on the mesoscale organization. We sort the blocks according to their column relative humidity (from low to high), allowing us to examine how the terms evolve in moisture-time space. Because of weak temperature gradients in the free troposphere, this is essentially equivalent to ranking blocks according to $\hat{h}'$.

[28] This analysis framework allows us to quantify and compare the feedbacks that play a role in self-aggregation. Examining each term in equation (9) as a function of time and column humidity allows us to investigate both the evolution to a self-aggregated state and its maintenance. We can also explain the anomalies of each diabatic term and thereby give a physical description of each relevant mechanism. Additionally, partitioning the surface flux anomalies allows us to isolate the wind surface flux feedback from the air-sea enthalpy disequilibrium surface flux feedback. We will then be able to clearly delineate the role of surface flux feedbacks in self-aggregation.

6. Results

[29] In order to determine which physical mechanisms are important for both the evolution and maintenance of self-aggregation, we investigate the evolution of the various feedback terms of equation (9) in both moisture and time space. First, we examine a Hovmuller plot of the sum of all the diabatic correlation terms, $\hat{h}'\text{SEF}'+\hat{h}'\text{NetSW}'+\hat{h}'\text{NetLW}'$, for the simulation at 305 K (Figure 4). For each day, we have normalized the diabatic correlation terms by the horizontal mean of the vertically integrated FMSE variance ($\{\hat{h}'^2\}$). Because $\hat{h}'^2$ increases with time, normalizing in this manner makes it easier to interpret what is happening in the early stage of aggregation, when both the vertically integrated FMSE anomalies and forcing terms are small. Note that the color bar in Figure 4 saturates; the maximum value in the dry regions at the beginning of the simulation is 2.3 day^{-1}. The sum of all the diabatic correlation terms is positive during the first 20 days of the
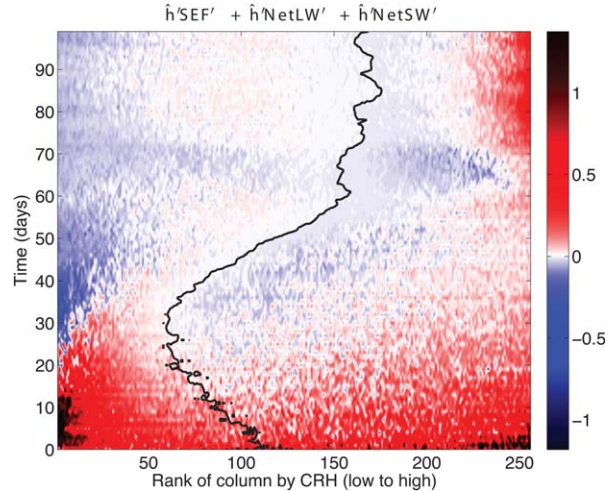

Figure 4. Sum of all diabatic correlation terms in vertically integrated FMSE spatial variance budget, normalized at each time by $\{\hat{h}'^2\}$. Plotted as a function of time (y axis) and moisture space (x axis), where each term has been averaged over a day and a 48×48 km^2 block, and has units of day^{-1}. On the x axis, dry regions are on the left and moist regions are on the right, sorted according to block-averaged column relative humidity (CRH). Results are from the simulation at 305 K. The black line is the $\hat{h}'=0$ contour. Note that the color bar saturates.

simulation. The strongest positive values occur in the driest regions over the first 10 days. With time, these positive values diminish and propagate toward moister regions, expanding the dry patch. This evolution is consistent with our earlier observation that the dry regions expand and eventually force all the convection into one cluster. In the moist regions, positive correlations persist through the simulation.

[30] We also note that the sum of all the diabatic correlation terms is negative at times and places throughout the simulation; competition between positive and negative feedbacks may explain why it takes so long for the cluster to fully form. In particular, the diabatic feedback terms are negative in the dry regions from day 30 to 50, but $\hat{h}'^2$ is still increasing in those regions over that time period (not shown). This indicates that the kinematic term, involving the horizontal convergence of the flux of vertically integrated FMSE, must be playing a role. Currently, we calculate this term as a residual from the rest of the $\hat{h}'^2$ budget due to the difficulties of calculating it directly from infrequent output. The contribution of the convergence term to the domain averaged $\hat{h}'^2$ budget is shown in Figure 5. The convergence of vertically integrated FMSE by the circulation is comparable in magnitude to the diabatic terms in the $\hat{h}'^2$ budget. In particular, the convergence term is positive from day 25 to 60, in the intermediate stages of self-aggregation. During this time, it amplifies vertically integrated FMSE anomalies, whereas in the early stages of aggregation it acts as a damping term. The finding that the convergence term plays an important role is consistent with *Bretherton et al.* [2005] and *Muller and*
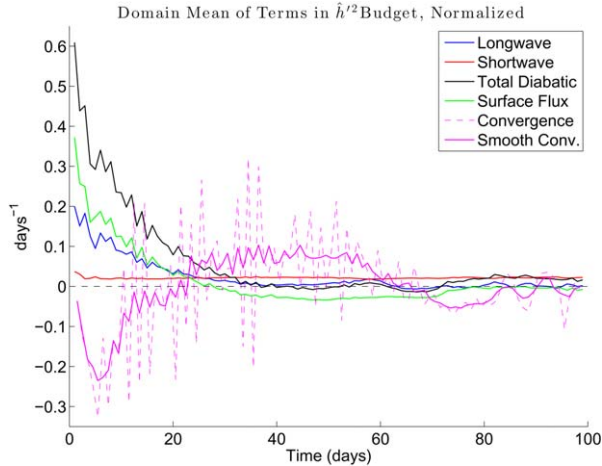
Figure 5. Time evolution of domain mean of terms in the $\hat{h}'^2$ budget, each normalized by $\{\hat{h}'^2\}$, with units of day^{-1}. Plotted is the sum of all diabatic correlation terms (black) and correlation between vertically integrated column FMSE anomalies and column longwave flux convergence (blue), column shortwave flux convergence (red), surface enthalpy flux (green), and horizontal convergence of flux of FMSE (pink dashed). A 5 day running average is applied to the horizontal convergence term to provide a smoothed version (solid pink). The black dashed line is the zero line, plotted as a reference.

Held [2012], who found that mesoscale circulations intensify the later stages of self-aggregation via an up gradient transfer of moist static energy, and will not be explored further here.

[31] The individual terms on the right side of equation (9), with the surface enthalpy flux broken down into wind and disequilibrium-dependent parts according to equation (10), are shown in Figure 6. We have again normalized each term by $\{\hat{h}'^2\}$. The color bar in each of the plots is the same (between -1.18 day^{-1} and 1.37 day^{-1}) to allow for easy comparison, but note that the color scale saturates in a few places. Figures 6a and 6b reinforce the notion of competition between positive and negative feedbacks, as the correlations of vertically integrated FMSE anomalies with the column radiative flux convergence anomalies are mostly positive during the first 60 days of the simulation (when the cluster is developing), while the correlations with the surface enthalpy flux anomalies are predominantly negative from day 20 to day 60. The total surface flux feedback (Figure 6b) is positive during the first 20 days of the simulation and is largest in the driest regions. One unexplained feature is the relatively abrupt transition around days 60 to 70.

[32] In Figures 6c–6f, the correlations are further decomposed. First, we examine the correlation between the vertically integrated FMSE anomalies and the column shortwave flux convergence anomalies (Figure 6e). This term is positive nearly everywhere, reflecting negative anomalies in NetSW in the dry regions (where $\hat{h}' < 0$) and positive anomalies in NetSW in the moist regions (where $\hat{h}' > 0$). This occurs simply because

water vapor is, after ozone, the most important shortwave absorber in the atmosphere.

[33] The sign of the correlation term involving column longwave flux convergence anomalies (Figure 6c) varies. In the first 20 days, the longwave term is positive, helping to amplify the developing dry patch. The column longwave flux convergence therefore must be more negative (more of a sink of energy) in the driest regions than elsewhere during that time period. Later, the longwave term is negative in the dry regions, indicating that at that time, the column longwave flux convergence must be less negative than average (less of a sink of energy) in the dry regions. Conversely, once the cluster is established (day 60 onward), the longwave term is a strong positive feedback in the moistest regions, and is the dominant contributor to the overall positive radiative feedback (Figure 6a) there. The physical mechanisms causing the longwave term to be a positive or negative feedback will be discussed in more detail in section 7.

[34] In regard to the surface flux term, we note that the correlation between vertically integrated FSME anomalies and the portion of the surface enthalpy flux anomalies that are due to wind speed anomalies (Figure 6d) is mostly positive. However, while the surface flux-wind feedback is a positive feedback for aggregation in our simulations, it is strongly counteracted by a negative surface flux feedback due to variations in the air-sea enthalpy disequilibrium (Figure 6f). Finally, while not shown here, the "eddy term" involving the correlation between vertically integrated FMSE anomalies and the product of wind speed and air-sea disequilibrium anomalies reflects that the wind speed and disequilibrium anomalies are anticorrelated. It is overall a negative feedback in the moist regions (where $\hat{h}' > 0$) and a positive feedback in the dry regions (where $\hat{h}' < 0$), and is the same order of magnitude but weaker than the other terms. Summing these components yields a total surface flux feedback that is positive in the early stages of aggregation, but negative most of the remainder of the simulation (Figure 6b).

[35] Finally, we note that all of these components of the diabatic terms have comparable magnitude, indicating that each physical process discussed above is important for self-aggregation. Analyzing these mechanisms in the framework of an $\hat{h}'^2$ budget allows us to quantify each process throughout the entire evolution of self-aggregation. Notably, the mechanisms that amplify the initial dry patch and control the evolution to an aggregated state are not necessarily the same as those that maintain the cluster once it is established, as was also suggested by *Muller and Held* [2012]. For example, the longwave radiative feedback is the strongest positive feedback from day 60 to 100, when there is a mature cluster. Shortwave radiation is the dominant positive diabatic feedack throughout the intermediate stage of aggregation, while longwave radiation and surface fluxes are the strongest positive feedbacks in the earliest stage (Figure 6). The strongest positive feedbacks in each stage of aggregation are summarized in Table 2.
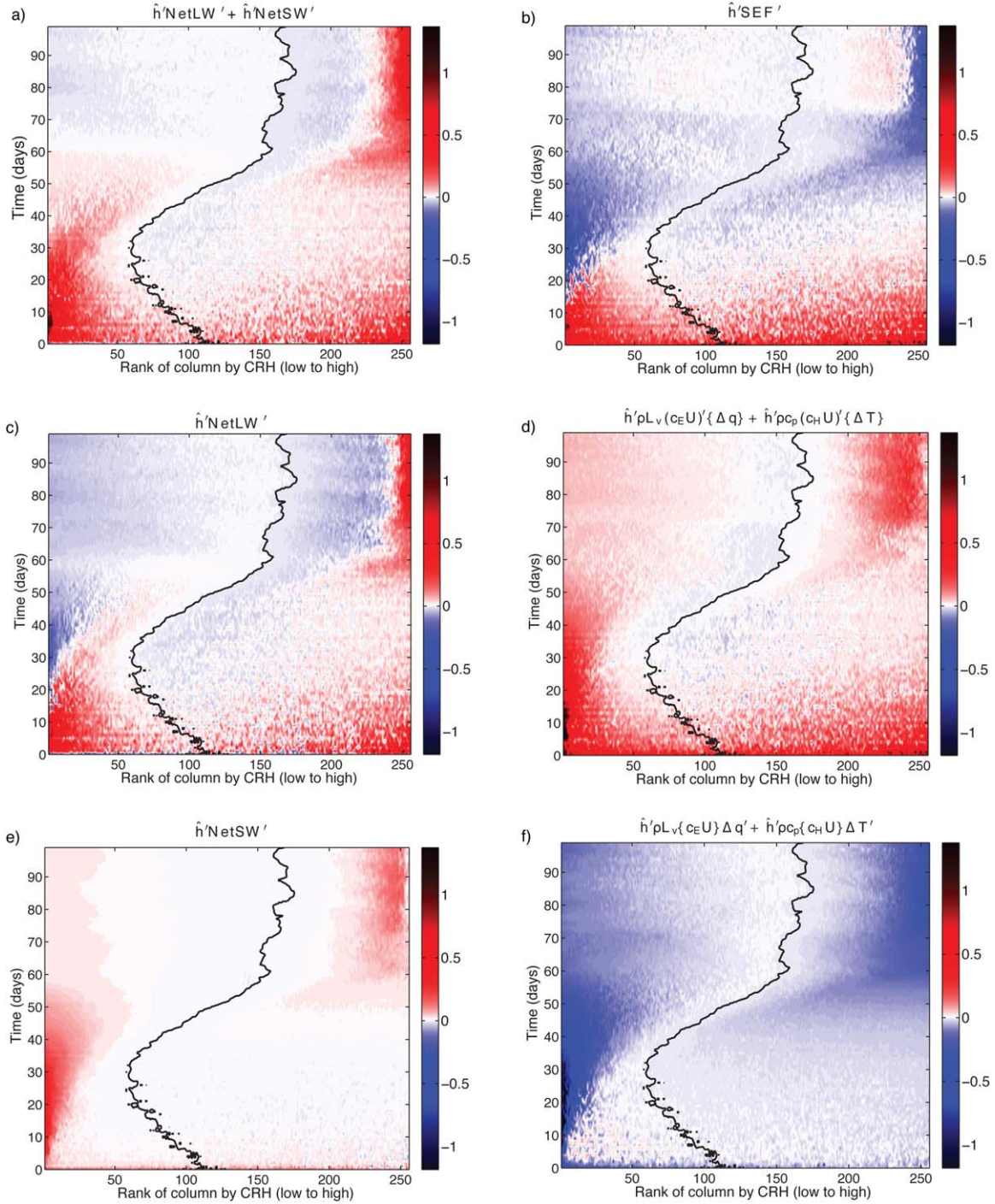
Figure 6. (left) Correlation between vertically integrated FMSE anomalies and column radiative flux convergence anomalies ((a) column radiative flux convergence, (c) column longwave convergence, (e) column shortwave convergence). (right) Correlation between vertically integrated FMSE anomalies and surface enthalpy flux anomalies ((b) total surface enthalpy flux anomaly, (d) anomaly due to surface wind speed anomalies, (f) anomaly due to air-sea enthalpy disequilibrium anomalies). All terms have been averaged over each day and over 48 × 48 km^2 blocks, normalized by $\{\hat{h}'^2\}$, are from the simulation at 305 K, and have units of day^{-1}. On the x axis, dry regions are on the left and moist regions are on the right, sorted according to block-averaged column relative humidity (CRH). The black line is the $\hat{h}' = 0$ contour, plotted as a reference. Note that the color bar saturates in a few places.

Table 2. Dominant Positive Feedbacks at Each Stage of Aggregation

Stage	Day	Feedback Term(s)
Early	0–20	Longwave radiation, surface fluxes
Intermediate	20–30	Shortwave radiation
Intermediate	30–60	Shortwave radiation, horizontal convergence
Mature	60–100	Longwave radiation

7. Discussion

7.1. Shortwave Radiation

[36] To focus on processes that amplify the initial dry patch, we look at time-height cross sections of the evolution of the driest block. It was shown in the previous section that the diabatic contribution to the intermediate stages of aggregation is dominated by the shortwave radiation term in the vertically integrated FMSE variance budget (equation (9)), due to reduced atmospheric absorption of shortwave radiation by water vapor in the dry regions compared to the moist regions. Figure 7 indicates that the upper troposphere dries out first, while the response of the shortwave heating rates to this perturbation is shown in Figure 8b. The shortwave heating rate is clearly reduced in the developing dry patch compared to its value at day one. Note that the shortwave heating rate is increased in the lower levels; this is because the reduced shortwave absorption aloft allows more of the shortwave radiative flux to reach the lower atmosphere.

[37] Clouds are capable of modulating the response of the shortwave heating rate to the development of the dry patch. However, the clear sky column shortwave flux convergence increases nearly as much as the total column shortwave flux convergence between dry and moist regions (Figure 9a), which indicates that the positive shortwave feedback is mostly a clear sky effect. The same is true in the mature phase of aggregation (Figure 10a). In the regions where there are low clouds at day 90 (Figure 11), the clouds act to increase the column shortwave flux convergence, as indicated by the locations in Figure 10a where the value of the red curve exceeds that of the blue curve. This is likely due to atmospheric absorption of reflected shortwave radiation. In contrast, the deep clouds in the very moistest regions block solar radiation from passing through much of the atmosphere, decreasing the column shortwave flux convergence.

7.2. Longwave Radiation

[38] The physical mechanisms controlling the longwave radiative feedback are less intuitive. Ignoring clouds for the moment, the column longwave flux convergence varies between dry and moist regions because variations in atmospheric water vapor determine variations in the longwave emissivity. To demonstrate the effect of decreasing the water vapor content of the atmosphere, we consider the behavior of the longwave radiative fluxes in a simple two-layer representation of

the atmosphere (Figure 12a). We assume that convection maintains a constant lapse rate of 6 K/km; this, combined with a fixed surface temperature, fixes the temperatures of the two atmospheric layers. The lower layer has an emissivity ϵ_1, which we take to be larger than that of the upper layer (ϵ_2) because water vapor decreases exponentially with altitude. The net upward longwave flux at the top of the atmosphere in this representation is

$$\text{LW}_{\text{TOA}} = \epsilon_2 \sigma T_2^4 + (1-\epsilon_2)\epsilon_1 \sigma T_1^4 + (1-\epsilon_2)(1-\epsilon_1)\sigma T_s^4, \tag{11}$$

where σ is the Stefan-Boltzmann constant., T_s is the surface temperature, T_1 is the temperature at which the lower layer emits longwave radiation, and T_2 is the temperature at which the upper layer emits longwave radiation. The first term in equation (11) is the flux upward from the second atmosphere layer. The second term is the flux upward from the first layer that is not absorbed by the second layer. The third term is the flux upward from the surface that is not absorbed by the first and second layers. The net upward longwave flux at surface is

$$\text{LW}_{\text{Sfc}} = \sigma T_s^4 - \epsilon_1 \sigma T_1^4 - (1-\epsilon_1)\epsilon_2 \sigma T_2^4. \tag{12}$$

The first term in equation (12) is the flux upward from the surface. The second term is the flux downward from the first atmosphere layer. The third term is the flux downward from the second layer that is not absorbed by the first layer. Subtracting equation (11) from equation (12) gives the equation for the column longwave flux convergence:
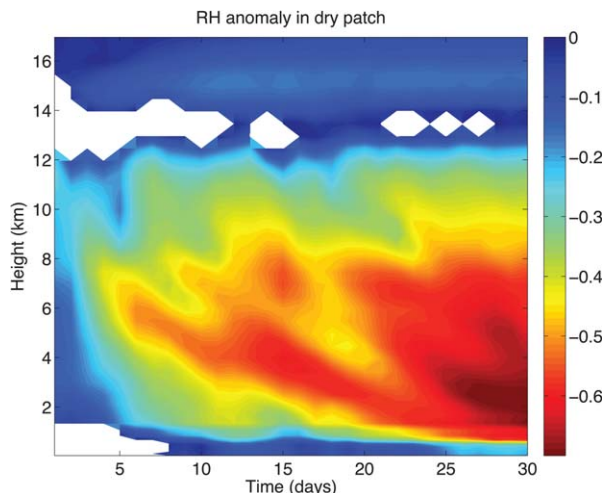

Figure 7. Height-time cross section of the relative humidity anomaly from the initial relative humidity profile over the first 30 days of the simulation at 305 K. The relative humidity anomaly plotted is from an average over the $48 \times 48 \text{ km}^2$ block that is the driest (according to column relative humidity) at day 10. White shading indicates positive values.
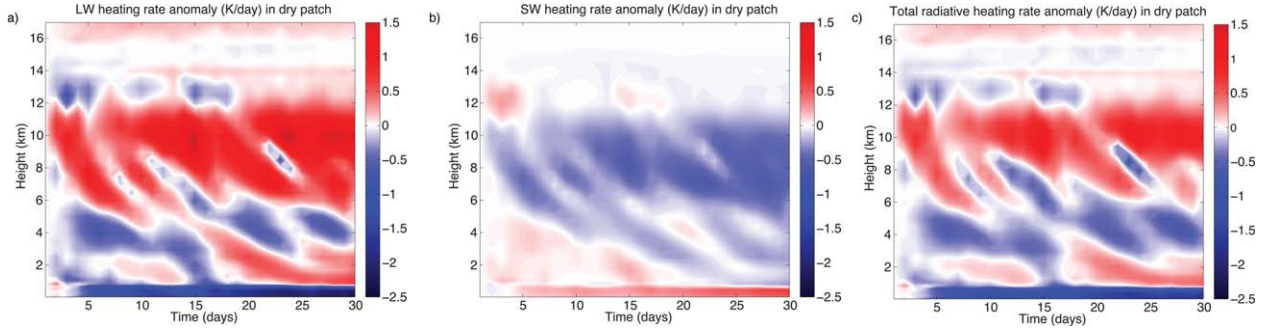
Figure 8. Height-time cross section of the (a) longwave, (b) shortwave, and (c) total radiative heating anomalies (K/day) over the first 30 days of the simulation at 305 K. The anomalies plotted are from an average over the 48 × 48 km^2 block that is the driest (according to column relative humidity) at day 10, and are anomalies from the profiles of (a) longwave, (b) shortwave, and (c) total radiative heating rates, respectively, in that block at day 1.

$$\text{LWFC} = \sigma T_1^4(\epsilon_1\epsilon_2 - 2\epsilon_1) + \sigma T_2^4(\epsilon_1\epsilon_2 - 2\epsilon_2)$$
$$+ \sigma T_s^4(\epsilon_1 + \epsilon_2 - \epsilon_1\epsilon_2). \tag{13}$$

Figure 12b shows the dependence of equation (13) on the emissivities of the upper and lower layers. The temperatures used in the calculation are 305, 275, and 245 K, for T_s, T_1, and T_2, respectively. The arrow from point A to point B is an example of a reduction in ϵ_1 and ϵ_2 that results in a decrease in the magnitude of column longwave cooling. The arrow from point C to point D also indicates a reduction in ϵ_1 and ϵ_2, but in this case, it results in an *increase* in the magnitude of column longwave cooling. Even in this very simple model the column longwave cooling is sensitive to how ϵ_1 and ϵ_2 are changed and what their value was initially. To understand the physical reason for this behavior, consider the two opposing effects of decreasing the water vapor content of the upper troposphere. One effect is that decreasing the water vapor decreases the longwave emissivity of the upper troposphere, which is a tendency toward less column longwave cooling. How-

ever, the remote effect of a decrease in the longwave emissivity of the upper troposphere is a decrease in the downward longwave flux to the lower troposphere. This reduces a source of energy for the lower troposphere and is thus a tendency toward more column longwave cooling. The balance of these two opposing effects in the column integral determines whether the longwave term can be either a positive or a negative feedback (Figure 6c).

[39] During the initial stages of aggregation, the longwave feedback is positive in the driest regions. Figure 8a shows that there is anomalous longwave heating in the middle and upper troposphere in the dry patch compared to its value at day one, which corresponds to decreased upper tropospheric water vapor (Figure 7). This response is opposed by anomalous longwave cooling in the lower troposphere which is evidently large enough to cause the longwave feedback to be slightly positive initially. Note that a positive anomaly indicates an *decrease* in the magnitude of longwave cooling because the longwave heating rate has a negative value. The longwave heating rate anomalies in the dry patch
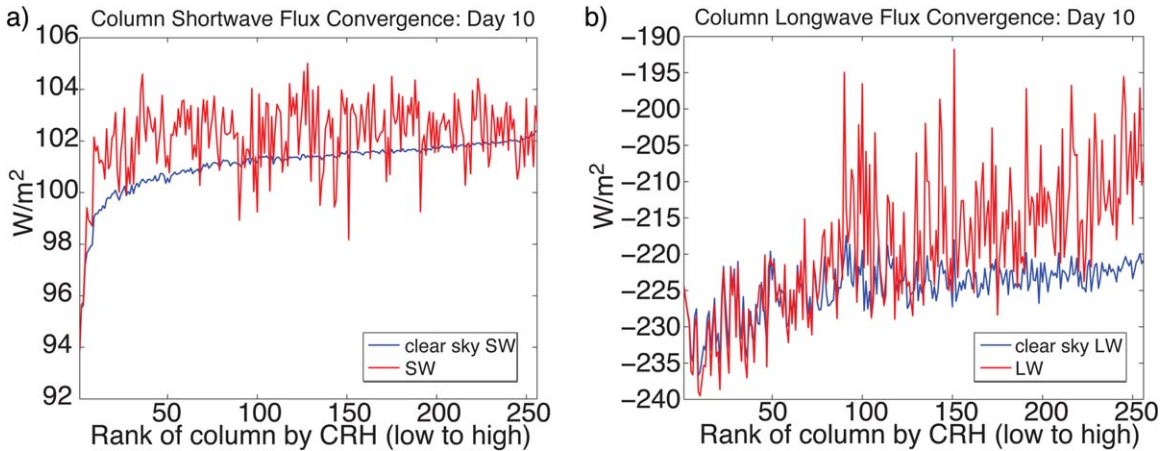

Figure 9. The total column (a) shortwave/(b) longwave radiative flux convergence (red) and clear sky (a) shortwave/(b) longwave column radiative flux convergence (blue). The quantities plotted have been block-averaged and sorted according to column relative humidity. The results shown here are from the day 10 mean of a simulation at an SST of 305 K.
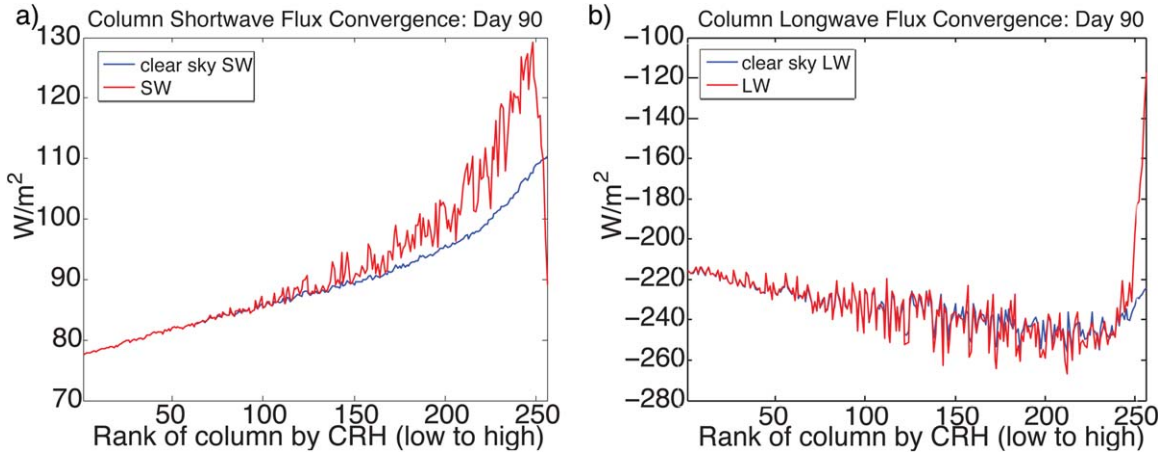
Figure 10. The total column (a) shortwave/(b) longwave radiative flux convergence (red) and clear sky (a) shortwave/(b) longwave column radiative flux convergence (blue). The quantities plotted have been block-averaged and sorted according to column relative humidity. The results shown here are from the day 90 mean of a simulation at an SST of 305 K.

(Figure 8a) are larger in magnitude than the shortwave heating rate anomalies (Figure 8b), so the total radiative heating rate anomalies tend to follow the pattern of the longwave anomalies (Figure 8c). The increased magnitude of clear sky column longwave convergence in the dry regions is similar to that of the total column longwave convergence, indicating it is primarily a clear sky, not cloud, effect (Figure 9b). Later in the simulation, as the dry perturbation amplifies and the lower troposphere also becomes drier, there is anomalous longwave heating of the lower levels due to the decreased low-level emissivity such that the total column longwave cooling is reduced in the dry regions. This is represented in Figure 6c as a transition (around day 30) from positive to negative values of the longwave feedback in the driest columns. A more complete description of this process, including the response of deep convection, will be provided in a companion paper [*Emanuel et al.*, 2013].

[40] Regarding the maintenance of the cluster once it exists, the longwave feedback is strongly positive in the very moistest regions where all the deep clouds are concentrated (Figure 11), primarily because the column longwave cooling is strongly reduced by the longwave opacity and low temperature of high clouds. The clear sky column longwave flux convergence (Figure 10b) also indicates slightly reduced longwave cooling in these regions, but is not nearly as large in magnitude as the reduction of longwave cooling by high clouds.

7.3. Surface Enthalpy Fluxes

[41] We noted in section 6 that the surface flux feedback due to variations in the surface wind speed (Figure 6d) was positive. The mechanism for this wind-induced surface heat exchange ("WISHE") feedback is that larger surface winds due to convective gustiness in the moist, intensely convecting regions enhance the surface fluxes there. The WISHE feedback in the early stages of

aggregation is strongest in the driest regions, while from day 70 onward it is strong near the edge of the mature cluster, (columns 200–240, in Figure 6b), which corresponds to the leading edge of the gust fronts propagating away from the center of the cluster. In each of these two areas, the positive WISHE feedback is able to overcome the negative air-sea enthalpy disequilibrium feedback and cause the total surface flux feedback to be positive. The mechanism governing the negative air-sea enthalpy disequilibrium feedback (Figure 6f) is straightforward. Because the simulations have a fixed, uniform
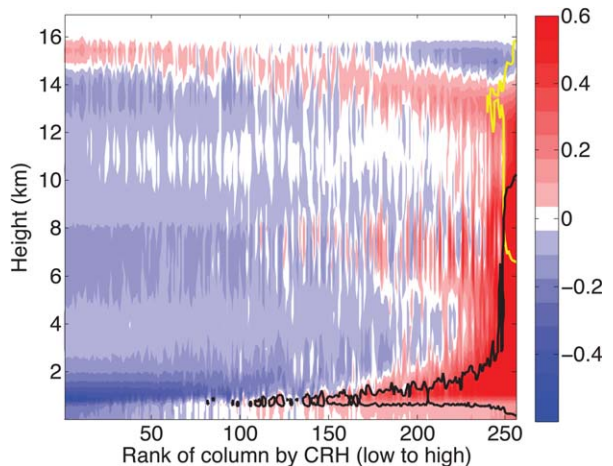

Figure 11. Anomalies from horizontal mean of relative humidity (shading) as a function of height and rank of column by CRH (low to high). Also plotted are the 0.01 g/kg contours of cloud ice condensate (yellow) and the 0.01 g/kg contours of cloud water condensate (black). The quantities plotted have been block-averaged and sorted according to column relative humidity. The results shown here are from the day 90 mean of a simulation at an SST of 305 K.
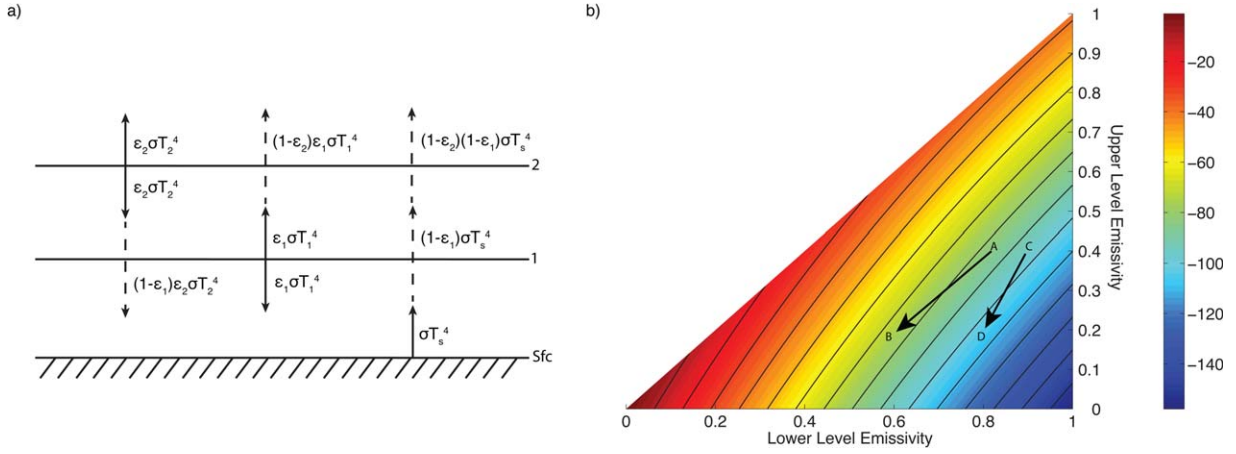
a)

b)

Figure 12. (a) Schematic representation of the longwave fluxes in a simple two-layer model of the atmosphere. Solid arrows represent fluxes from the indicated layer, dashed arrows represent the part of those fluxes that is transmitted through the adjacent layer(s). (b) This shows the column longwave radiative flux convergence (color contours, in W/m^2) calculated based on the schematic in Figure 12a, as a function of the lower level and upper level emissivities. The area of the graph where the upper level emissivity is larger than the lower level emissivity is omitted because it is unphysical. The black contours also indicate the column longwave convergence, but are plotted only every 10 W/m^2 to aid in visual interpretation. The points indicated by "A," "B," "C," and "D" and the arrows connecting them show the response to a hypothetical perturbation of the emissivities.

sea surface temperature and the surface enthalpy flux is dominated by the latent heat component, the air-sea enthalpy disequilibrium primarily depends on the boundary layer water vapor mixing ratio. The boundary layer water vapor mixing ratio is larger in the moist regions, where $\hat{h}'$ is positive, than the dry regions. The air-sea disequilibrium is anomalously negative in the moist regions, suppressing surface fluxes there.

8. Summary and Future Directions

[42] In this study, we introduce a novel approach to analyze the various physical mechanisms that play a role in the self-aggregation of convection in radiative-convective equilibrium simulations in a cloud-system resolving model. Since the column radiative flux convergence and surface enthalpy fluxes are diabatic sources and sinks of vertically integrated frozen moist static energy, using a budget of the spatial variance of vertically integrated FMSE allows us to quantify the radiative and surface flux feedbacks in a simulation that self-aggregated. Additionally, partitioning the surface enthalpy flux anomalies into a part due to surface wind speed anomalies, a part due to air-sea enthalpy disequilibrium anomalies, and an eddy term involving the product of the wind speed and air-sea disequilibrium anomalies enables us to determine the role of each separately in the surface flux feedback.

[43] A key finding is that all the terms in the $\hat{h}'$ budget are of similar magnitude, so shortwave radiative feedbacks, longwave radiative feedbacks, and surface flux feedbacks are all important for self-aggregation. The shortwave radiative feedback is a key positive feedback throughout the evolution of self-aggregation and is due

to increased absorption of water vapor by atmospheric water vapor in the moist regions compared to the dry regions. The longwave radiative feedback is initially a positive feedback in the dry regions, but is later negative. This is because the response of longwave cooling to a dry perturbation has two opposing effects, the net result of which varies in both space and time in our simulations. The surface flux feedback is positive during the first 20 days of the simulation, but is otherwise negative due to a strongly negative surface flux-enthalpy disequilibrium feedback which is only partially counteracted by a positive surface flux-wind (WISHE) feedback. Without the WISHE feedback, which is of comparable magnitude to the radiative feedbacks, the total surface flux feedback would be very strongly negative (perhaps negative enough to prevent, or at least, slow down, self-aggregation). In contrast to the evolution of self-aggregation, during which all the different feedbacks are relevant, the longwave cloud-radiation feedback dominates in the moistest regions during the time at which there is a mature cluster. Therefore, this study provides additional evidence for a distinction between feedbacks that maintain a cluster, and feedbacks that establish one. Our approach is valuable because it elucidates the relevant feedbacks during all stages of aggregation. Finally, while this study focused on the diabatic mechanisms controlling self-aggregation, we noted that the horizontal convergence of vertically integrated FMSE is also an important positive feedback during the intermediate stages of aggregation.

[44] The fact that the longwave feedback can be positive or negative depending on the balance of the two opposing responses to a dry perturbation suggests it as

13

a candidate for explaining the temperature dependence of self-aggregation. This will be thoroughly investigated in a companion paper [*Emanuel et al.*, 2013].

References

Arakawa, A., and W. Schubert (1974), Interaction of a cumulus cloud ensemble with the large-scale environment, Part I, *J. Atmos. Sci.*, *31*, 674–701.

Bretherton, C., P. Blossey, and M. Khairoutdinov (2005), An energy-balance analysis of deep convective self-aggregation above uniform SST, *J. Atmos. Sci.*, *62*, 4237–4292.

Challa, M., and R. Pfeffer (1990), Formation of Atlantic hurricanes from cloud clusters and depressions, *J. Atmos. Sci.*, *47*, 909–927.

Clough, S., M. Shephard, E. Mlawer, J. Delamere, M. Iacono, K. Cady-Pereira, S. Boukabara, and P. Brown (2005), Atmospheric radiative transfer modeling: A summary of the AER codes, *J. Quant. Spectrosc. Radiat. Transfer*, *91*, 233–244.

Computational, and Information Systems Laboratory (2012), Yellowstone: IBM iDataPlex System (University Community Computing), Natl. Cent. for Atmos. Res., Boulder, Colo. [Available at http://n2t.net/ark:/85065/d7wd3xhc].

Emanuel, K., A. A. Wing, and E. Vincent (2013), Radiative-convective instability, *J. Adv. Model. Earth Syst.*, *5*, doi:10.1002/2013MS000270.

Futyan, J., and A. Del Genio (2007), Deep convective system evolution over Africa and the tropical Atlantic, *J. Clim.*, *20*, 5041–5060.

Held, M. I., R. S. Hemler, and V. Ramaswamy (1993), Radiative-convective equilibrium with explicity two-dimensional moist convection, *J. Atmos. Sci*, *50*, 3909–3927.

Houze, R. (1977), Structure and dynamics of a tropical squall-line system, *Mon. Weather Rev.*, *105*, 1540–1567.

Houze, R., Jr. (2004), Mesoscale convective systems, *Rev. Geophys.*, *42*, RG4003, doi:10.1029/2004RG000150.

Iacono, M., J. Delamere, E. Mlawer, M. Shephard, S. Clough, and W. Collins (2008), Radiative forcing by long-lived greenhousegases: Calculations with the AER radiative transfer models, *J. Geophys. Res.*, *113*, D13103, doi:10.1029/2008JD009944.

Islam, S., R. Bras, and K. Emanuel (1993), Predictability of mesoscale rainfall in the tropics, *J. Appl. Meteorol.*, *32*, 297–310.

Jeevanjee, N., and D. M. Romps (2013), Convective self-aggregation, cold pools, and domain size, *Geophys. Res. Lett.*, *40*, 994–998, doi:10.1002/grl.50204.

Khairoutdinov, M., and K. Emanuel (2010), Aggregation of convection and the regulation of tropical climate, paper presented at 29th Conference on Hurricanes and Tropical Meteorology, Am. Meteorol. Soc., Tucson, Ariz.

Khairoutdinov, M., and K. Emanuel (2012), The effects of aggregated convection in cloud-resolved radiative-convective equilibrium, paper presented at 30th Conference on Hurricanes and Tropical Meteorology, Am. Meteorol. Soc., Ponte Vedra Beach, Fla.

Khairoutdinov, M., and D. Randall (2003), Cloud resolving modeling of the ARM summer 1997 IOP: Model formulation, results, uncertainties, and sensitivities, *J. Atmos. Sci.*, *60*, 607–625.

Lee, C. (1989), Observational analysis of tropical cyclogenesis in the western North Pacific. Part I: Structural evolution of cloud clusters, *J. Atmos. Sci.*, *46*, 2580–2598.

Machado, L., and W. Rossow (1993), Structural characteristics and radiative properties of tropical cloud clusters, *Mon. Weather Rev.*, *121*, 3234–3260.

Madden, R., and P. Julian (1971), Detection of a 40–50 day oscillation in the zonal wind in the tropical pacific, *J. Atmos. Sci.*, *28*, 702–708.

Maddox, R. (1980), Mesoscale convective complex, *Bull. Am. Meteorol. Soc.*, *61*, 1374–1387.

Mapes, B., and R. Houze Jr. (1993), Cloud clusters and superclusters over the oceanic warm pool, *Mon. Weather Rev.*, *121*, 1398–1415.

Mapes, B., R. Milliff, and J. Morzel (2009), Composite life cycle of maritime tropical mesoscale convective systems in scatterometer and microwave satellite observations, *J. Atmos. Sci.*, *66*, 199–208.

Mlawer, E., S. Taubman, P. Brown, M. Iacono, and S. Clough (1997), Radiative transfer for inhomogeneous atmospheres: RRTM, a validated correlated-k model for the longwave, *J. Geophys. Res.*, *102*, 16,663–16,682.

Muller, C., and I. Held (2012), Detailed investigation of the self-aggregation of convection in cloud resovling simulations, *J. Atmos. Sci.*, *69*, 2551–2565.

Nesbitt, S., E. Zipser, and D. Cecil (2000), A census of precipitation features in the tropics using TRMM: Radar, ice scattering, and lightning observations, *J. Clim.*, *13*, 4087–4106.

Nolan, D., E. Rappin, and K. Emanuel (2007), Tropical cyclonegenesis sensitivity to environmental parameters in radiative-convective equilibrium, *Q. J. R. Meteorol. Soc.*, *133*, 2085–2107.

Robe, F., and K. Emanuel (2001), The effect of vertical wind shear on radiative-convective equilibrium states, *J. Atmos. Sci*, *58*, 1427–1445.

Simpson, J., E. Ritchie, G. Holland, J. Halverson, and S. Stewart (1997), Mesoscale interactions in tropical cyclone genesis, *Mon. Weather Rev.*, *125*, 2643–2661.

Stephens, G., S. van den Heever, and L. Pakula (2008), Radiative-convective feedbacks in idealized states of radiative-convective equilibrium, *J. Atmos. Sci.*, *65*, 3899–3916.

Tobin, I., S. Bony, and R. Roca (2012), Observational evidence for relationships between the degree of aggregation of deep convection, water vapor, surface fluxes, and radiation, *J. Clim.*, *25*, 6885–6904.

Tompkins, A. (2001), Organization of tropical convection in low wind shears: The role of water vapor, *J. Atmos. Sci.*, *58*, 529–545.

Tompkins, A., and G. Craig (1998), Radiative-convective equilibrium in a three-dimensional cloud-ensemble model, *Q. J. R. Meteorol. Soc.*, *124*, 2073–2097.

Wing, A., and K. Emanuel (2012), Organization of tropical convection: Dependence of self-aggregation on SST in an idealized modeling study, paper presented at 30th Conference on Hurricanes and Tropical Meteorology, Am. Meteorol. Soc., Ponte Vedra Beach, Fla.

Corresponding author: A. A. Wing, Department of Earth, Atmospheric and Planetary Sciences, Massachusetts Institute of Technology, 54-1815, 77 Massachusetts Ave., Cambridge, MA 02139, USA. (awing@mit.edu)